Effects of high-order anharmonicity on anomalous lattice dynamics and thermal transport in fully filled skutterudite YbFe$_4$Sb$_{12}$

Jiongzhi Zheng,[1] Dongliang Shi,[2] Sijing Liu,[1] Yuewang Yang,[1] Chongjia Lin ⬤,[1] Zheng Chang ⬤,[3]
Ruiqiang Guo,[4,*] and Baoling Huang ⬤[1,5,6,†]

[1]*Department of Mechanical and Aerospace Engineering, The Hong Kong University of Science and Technology,
Clear Water Bay, Kowloon, Hong Kong*
[2]*Department of Land Surveying and Geo-Informatics, The Hong Kong Polytechnic University, Hung Hom, Kowloon, Hong Kong*
[3]*Key Laboratory of Ocean Energy Utilization and Energy Conservation of Ministry of Education, School of Energy and Power Engineering,
Dalian University of Technology, Dalian 116024, China*
[4]*Thermal Science Research Center, Shandong Institute of Advanced Technology, Jinan, Shandong 250103, China*
[5]*HKUST Foshan Research Institute for Smart Manufacturing, Hong Kong University of Science and Technology,
Clear Water Bay, Kowloon, Hong Kong*
[6]*HKUST Shenzhen-Hong Kong Collaborative Innovation Research Institute, Futian, Shenzhen 518055, China*

Accurately describing the lattice dynamics and microscopic mechanism of thermal transport in materials with low-lying flat phonon modes remains an outstanding challenge due to the intrinsic strong anharmonicity. In this paper, we investigate the lattice dynamics and thermal transport in skutterudite YbFe$_4$Sb$_{12}$ using a state-of-the-art first-principles-based anharmonic phonon renormalization technique and a unified theory of lattice thermal transport. In contrast to the previous phenomenological models that introduce additional resonant scattering terms or hopping channels, we show that the unusual total lattice thermal conductivity in YbFe$_4$Sb$_{12}$ can be accurately predicted by considering anharmonic phonon renormalization and coherence contributions from the off-diagonal terms of heat flux operators. Both the cubic and quartic anharmonicities are essential for precisely predicting the significant shift in phonon energies. Specifically, the anharmonicity-induced phonon stiffening of the low-lying flat modes significantly enhances the thermal conductivity of particlelike phonons, e.g., by up to a factor of 1.6 at 300 K, by suppressing the cubic coupling strength and altering the scattering phase space, resulting in much-improved agreement with experiments. By further including the coherence contributions, the predicted total thermal conductivity increases by ∼22% throughout the entire temperature range, reproducing well the experimental values in both magnitude and temperature dependence. In this paper, we highlight the strong impact of higher-order anharmonicity on lattice dynamics and thermal transport in the filled skutterudite YbFe$_4$Sb$_{12}$. The insights gained in this paper will be helpful for manipulating the thermal properties of skutterudites and potentially other complex materials with strong anharmonicity, which can improve their performance in applications such as thermoelectrics, ferroelectrics, and photovoltaics.

I. INTRODUCTION

The phonon-glass electron-crystal (PGEC) paradigm proposed by Slack [1], i.e., low thermal conductivity as in a glass in combination with good electronic properties as in a crystal [2], plays a crucial role in the selection of thermoelectric materials. Skutterudites are a class of thermoelectric materials showing PGEC characteristics and have long been considered promising candidates for intermediate-temperature heat-to-electricity conversion. They have a unique cagelike structure that can be filled with guest atoms, offering a great opportunity to optimize electronic and thermal properties. Filling the cages can largely reduce lattice thermal conductivity k_L, which is typically the major reason for enhanced thermoelectric efficiency [3–8]. Among the skutterudites, the fully filled

skutterudite YbFe$_4$Sb$_{12}$ has drawn vast attention due to its interesting magnetic and electrical properties [9–12] and ultra-low k_L [12,13]. Many efforts [14–16] have been devoted to understanding the suppressed thermal transport in YbFe$_4$Sb$_{12}$ in the past decade. However, the theory accurately describing thermal transport in YbFe$_4$Sb$_{12}$ is still up for debate.

The Peierls-Boltzmann transport equation (PBTE) [17,18] within a well-defined phonon picture, despite its success in precisely predicting the k_L of many crystals [19,20], was recently found to seriously underestimate the k_L in YbFe$_4$Sb$_{12}$ by 69.5% [13,14]. This finding questions the validity of the phonon picture. Mukhopadhyay *et al.* [15] argued that this underestimation arises from the ill-defined phonons and proposed a hopping channel to account for the k_L mainly contributed by those ill-defined phonons in YbFe$_4$Sb$_{12}$ and Tl$_3$VSe$_4$. However, the hopping channel is modeled by the harmonic approximation (HA) and simplified approximate method, i.e., models of Einstein [21] or Cahill *et al.* [22]. In another work, using the temperature-dependent effective

*ruiqiang.guo@iat.cn
†mebhuang@ust.hk

potential (TDEP) method [23], Wang *et al.* [16] further considered the effect of temperature on interatomic interactions for the prediction but overestimated κ_L in YbFe$_4$Sb$_{12}$ by 50%. They attributed the discrepancy between the prediction and experiment to resonant phonon scattering, although this resonant scattering mechanism has been questioned by several experimental and theoretical studies in skutterudites [4,24] and clathrates [25].

The previously introduced resonant scattering terms or heat transfer channels are phenomenological, although they can make the predicted k_L agree well with the experimental values [15,16]. Whether these phenomenological models capture the real physical picture remains elusive considering the limitations of previous calculation approaches. Specifically, all those calculations ignored the influence of either anharmonicity-induced phonon renormalization or coherent thermal transport channel, which has been demonstrated to be very important for predicting k_L of highly anharmonic or/and complex compounds. For instance, Simoncelli *et al.* [26] successfully explained thermal transport in CsPbBr$_3$ using a derived unified theory of thermal transport that couples phonon and coherence contributions. Tadano and Tsuneyuki [27] reproduced the experimental lattice thermal conductivity in Ba$_8$Ga$_{16}$Ge$_{30}$ by considering temperature-induced phonon hardening of the low-lying optical modes resulting from the quartic anharmonicity. Xia *et al.* [28] unraveled the microscopic mechanism of thermal transport in cubic Cu$_{12}$Sb$_4$S$_{13}$ tetrahedrites by considering the temperature effect, phonon, as well as coherence contributions.

In this paper, we investigate the anharmonic lattice dynamics and multichannel thermal transport in skutterudite YbFe$_4$Sb$_{12}$ using first-principles calculations based on the density functional theory (DFT). We implemented the anharmonic phonon renormalization considering the cubic and quartic anharmonicities using a perturbative manner and self-consistent phonon (SCP) theory, respectively, and explored the microscopic origin of the phonon stiffening. Using the harmonic/renormalized anharmonic frequencies and eigenvectors, we calculated k_L using the PBTE and a unified theory of thermal transport combining the diagonal and off-diagonal terms of the heat-flux operators (OD) in YbFe$_4$Sb$_{12}$. Our calculations illustrate that the continuous phonon stiffening of the Yb-dominated low-lying flat modes associated with the lattice anharmonicity suppresses the cubic coupling strength and alters the scattering phase space (SPS), thereby resulting in a significant enhancement in phonon thermal transport. By further evoking the coherent thermal transport channel, we can reproduce well the experimentally measured k_L in YbFe$_4$Sb$_{12}$ both in magnitude and temperature dependence. The unified theory of thermal transport incorporating population (phonon channel) and coherence (coherent channel) contributions with phonon renormalization technique will facilitate a deeper understanding of skutterudites and potentially other complex materials.

II. COMPUTATIONAL MODELING

All the DFT calculations in this paper were performed with the projector-augmented wave (PAW) method [29], as implemented in the Vienna *Ab initio* Simulation Package [30–33]. The PAW Perdew-Burke-Ernzerhof (PBE) [34] pseudopo-

tentials were used for the exchange-correlation functional because they can predict well the lattice parameters and phonon properties of YbFe$_4$Sb$_{12}$ according to our test. The PBE functional has also been used by previous work [14]. A cubic unit cell of the fully filled skutterudite YbFe$_4$Sb$_{12}$ with the space group $Im\bar{3}$ was employed for structural optimization [see Fig. 1(a)]. The optimized lattice constant $a = 9.17$ Å is in good agreement with the experimental value $a = 9.16$ Å [13]. Considering that thermal expansion of the skutterudite YbFe$_4$Sb$_{12}$ is small [35], we did not consider the effect of thermal expansion on thermal properties in the current calculation. A $2 \times 2 \times 2$ supercell containing 272 atoms was used for static phonon calculations, mapping out potential energy surfaces (PESs), and *ab initio* molecular dynamics simulation.

The original harmonic interatomic force constants (IFCs) were extracted by the finite-displacement approach [36]. The higher-order anharmonic IFCs, i.e., cubic and quartic IFCs, were estimated using the compressive sensing lattice dynamics method [37] based on the limited precise displacement-force datasets. All terms of harmonic IFCs were included, while the cutoff radii for cubic and quartic IFCs were set to 6.35 and 5.29 Å, respectively.

To renormalize phonon energies at finite temperatures, the SCP [38–44] theory was used to calculate the frequency shifts from quartic anharmonicity (loop diagram). The resultant temperature-dependent anharmonic frequencies $\Omega_{qj}(T)$ and polarization vectors $\varepsilon_{\mathbf{q}j}(T)$ can be estimated by diagonalizing the following matrix $V_{\mathbf{q}}$ given as

$$V_{\mathbf{q}jj'} = \omega_{\mathbf{q}j}^2 \delta_{jj'} + \frac{1}{2} \sum_{q''} \Phi(\mathbf{q}j; -\mathbf{q}j'; q''; -q'') \langle Q_{q''}^* Q_{q''} \rangle,$$
(1)

$$\langle Q_{q''}^* Q_{q''} \rangle = \left(\frac{\hbar}{2\Omega_{q''}} \right) [1 + 2n(\Omega_{q''})],$$
(2)

where $\omega_{\mathbf{q}j}$ refers to the harmonic phonon frequency associated with the wave vector $\mathbf{q}$ and phonon branch j. Here, $\langle Q_{q''}^* Q_{q''} \rangle$ represents the mean-square displacement (MSD) of the normal coordinate Q. Also, the q in the expression denotes the shorthand notation for a composite index of the wave vector and phonon branch $(\mathbf{q}, j)$ and satisfying $q = (\mathbf{q}, j)$ and $-q = (-\mathbf{q}, j)$. Furthermore, $\Phi(\mathbf{q}j; -\mathbf{q}j'; q''; -q'';)$ is the reciprocal representation of 4$^{\text{th}}$-order IFCs in real space and $n(\omega) = 1/[e^{(\hbar\omega/k_B T)} - 1]$ is the Bose-Einstein distribution (k_B, $\hbar$ are the Boltzmann and reduced Planck constants, respectively).

Based on the first-order SCP calculations, the anharmonic phonon renormalization from the second-order contributions due to the bubble diagram can be evaluated in a perturbative manner through [28,45]

$$\Delta_q^B = -\frac{1}{\hbar} \text{Re} \sum_q^B (\Omega_q),$$
(3)

$$\sum_q^B (\Omega_q) = \frac{1}{2\hbar} \sum_{q_1, q_2, s=\pm 1} |V_3(-q; q_1; q_2)|^2$$
$$\times \left(\frac{n_1 + n_2 + 1}{s\Omega_c + \Omega_{q_1} + \Omega_{q_2}} - \frac{n_1 - n_2}{s\Omega_c + \Omega_{q_1} - \Omega_{q_2}} \right).$$
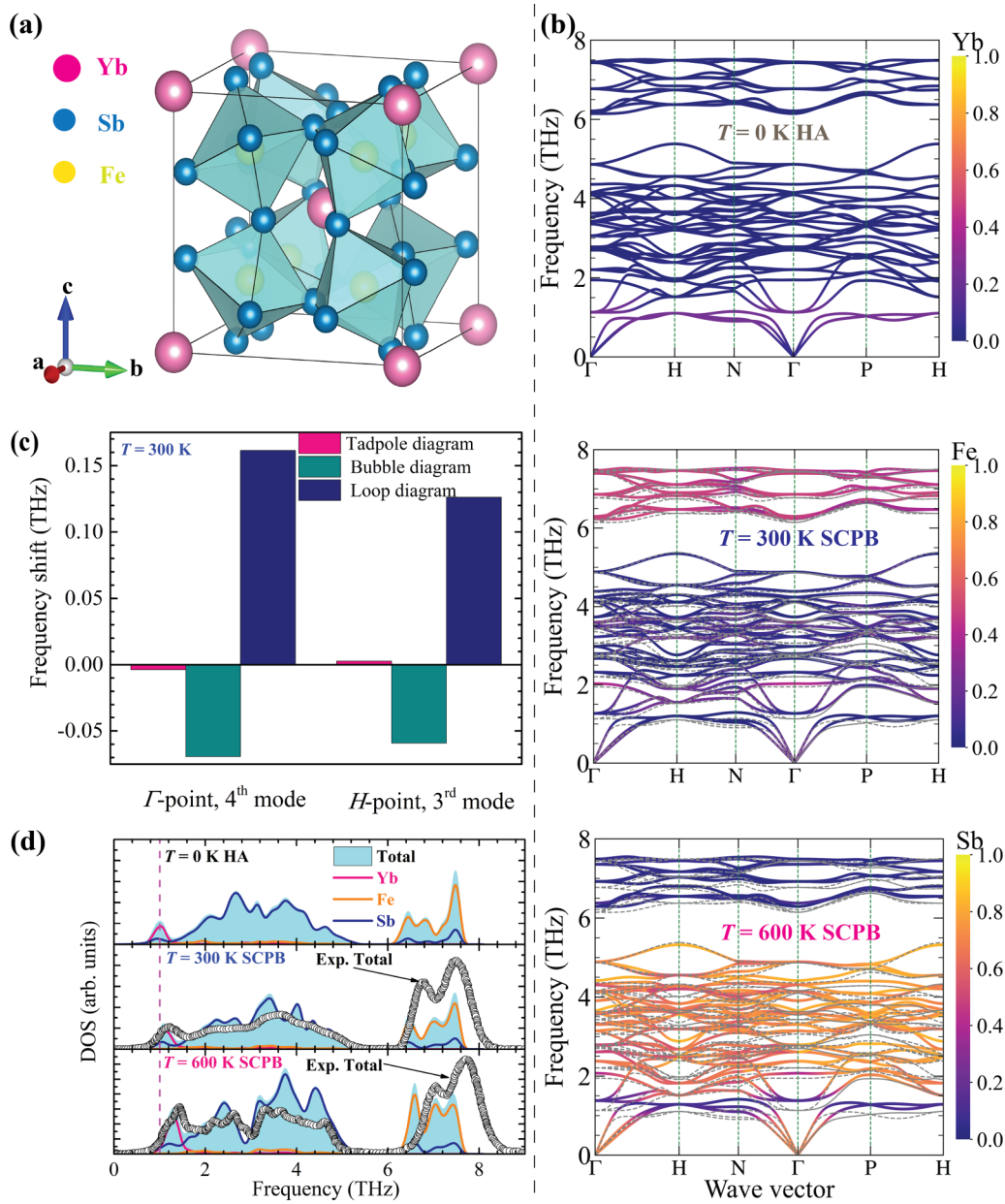(4)

FIG. 1. (a) Crystal structure of skutterudite $YbFe_4Sb_{12}$ conventional cell, which features a sublattice formed by $FeSb_6$ octahedral units with Yb atoms. Yb, Sb, and Fe atoms are colored in pink, blue, and yellow, respectively. (b) Calculated phonon dispersion curves along some high-symmetry paths in the Brillouin zone. Top panel: Within the harmonic approximation (HA) method, and all bands are colored according to the atomic participation ratio of atom Yb. Middle panel: Within the self-consistent phonon + bubble (SCPB) method at $T = 300$ K, and all bands are colored according to the atomic participation ratio of atom Fe. The dashed lines depict the phonon dispersions calculated using the HA method. Bottom panel: The same as the middle panel but at $T = 600$ K and the atomic participation ratio of atom Sb. (c) Calculated frequency shifts ascribing from tadpole, bubble, and loop diagrams for the fourth mode at the Γ point and the third mode at the H point in the Brillouin zone, respectively. (d) Atom-projected and total phonon density of states with (300 and 600 K) and without (0 K) considering anharmonic phonon renormalization, in comparison with those obtained from experiments at corresponding temperatures [66,67].

Here, Δ_q^B is the frequency shift due to the bubble diagram, Ω_q is the renormalized phonon frequency due to the loop diagram, $\sum_q^B(\Omega_q)$ is the phonon frequency-dependent bubble self-energy, $\Omega_c = \Omega_q + i0^+$ with 0^+ being a positive infinitesimal, and V_3 is the three-phonon interaction. Note that we denote SCP + bubble diagram (SCPB) as a shorthand notation

for the above treatment of anharmonic phonon renormalization in this paper.

Based on the obtained harmonic and anharmonic IFCs, the lattice thermal conductivity k_L was calculated by a unified theory of thermal transport incorporating population and coherence contributions [26]. The resulting formula for k_L takes

the form of

$$\kappa_L^{P/C} = \frac{1}{NV} \sum_{\mathbf{q}jj'} \frac{c_{\mathbf{q}j}\omega_{\mathbf{q}j'} + c_{\mathbf{q}j'}\omega_{\mathbf{q}j}}{\omega_{\mathbf{q}j} + \omega_{\mathbf{q}j'}} \upsilon_{\mathbf{q}jj'}$$

$$\otimes \upsilon_{\mathbf{q}j'j} \frac{\Gamma_{\mathbf{q}j} + \Gamma_{\mathbf{q}j'}}{(\omega_{\mathbf{q}j} - \omega_{\mathbf{q}j'})^2 + (\Gamma_{\mathbf{q}j} + \Gamma_{\mathbf{q}j'})^2}, \quad (5)$$

where the superscripts P and C represent the phonon and coherence contributions, respectively, $c_{\mathbf{q}j}$ is the mode-specific heat associated with wave vector $\mathbf{q}$ and phonon branch j, V is the primitive-cell volume, $\omega_{\mathbf{q}j}$ is the phonon frequency, $\Gamma_{\mathbf{q}j}$ is the phonon linewidth, and $\upsilon_{\mathbf{q}}$ is the phonon group velocity. The diagonal term ($j = j'$) gives the population contribution (Peierls' contribution), whereas the off-diagonal term ($j \neq j'$) gives rise to the coherence contribution. The total lattice thermal conductivity is then given as $\kappa_L = \kappa_L^P + \kappa_L^C$. Note that we found that the difference of the κ_L^P calculated by the single-mode relaxation time approximation (RTA) and an iterative solution of the PBTE is negligible. All the main phonon calculations and the IFC extraction were performed using the ALAMODE package [20,38]. See the Supplemental Material (SM) [46] for the full computational details and methodology (see also Refs. [47–65] therein).

III. RESULTS AND DISCUSSION

A. Lattice dynamics and anharmonicity

We start by comparing the calculated phonon dispersion curves of YbFe$_4$Sb$_{12}$ using the HA method and the SCPB method at 0, 300, and 600 K [see Fig. 1(b)]. We implemented the anharmonic phonon renormalization at finite temperatures using the SCPB method which considers both the cubic (bubble self-energy included) and quartic (loop self-energy included) anharmonicities. The calculated phonon dispersions based on the HA are in good agreement with previous work [14]. Upon including anharmonic phonon renormalization, an overall significant phonon stiffening occurs for the low-lying flat modes with frequencies ∼1 THz. By projecting the atomic participation ratio onto the phonon branches, we find that the low-lying flat modes are mainly dominated by the vibrations of Yb atoms. This feature is also reflected by the atom-decomposed partial density of states (PDOS) in Fig. 1(d) and is consistent with the experimental observations [35]. The calculated Yb-dominated PDOS peak shifts by ∼0.06 THz from 10 to 300 K, agreeing favorably with the experimental result (∼0.1 THz) [35] (see Figs. S1(a) and S1(b) in the SM [46]). Different from the continuous phonon stiffening of the Yb-dominated modes, the Sb-dominated intermediate-frequency modes undergo various shifts, including the relatively weak stiffening for the majority modes, phonon softening at the H symmetry point for the minority modes, and the negligible phonon softening for the highest Sb-dominated modes [see Fig. 1(b)].

We next evaluated how the frequency shifts depend on the tadpole, bubble, and loop diagrams [45]. Figure 1(c) shows the frequency shifts in the low-lying flat modes are mainly induced by the bubble and loop diagrams, while the tadpole diagram-induced frequency shift is minor and negligible. The subsequent analysis will show that the frequency

shifts resulting from both the bubble and loop self-energy are necessary for reproducing the experimental results of YbFe$_4$Sb$_{12}$. Meanwhile, we note that the frequency shifts resulting from the bubble diagram are quite significant in some compounds [28,44] but can be neglected in other materials [27].

Figure 1(d) shows the calculated phonon density of states (DOS) in comparison with the experimental results at finite temperatures [66,67]. Compared with the harmonic DOS, the calculated anharmonic DOSs at 300 and 600 K agree well with experiments [66,67]. Specifically, within the HA framework, the vibrational Yb-dominated peak ∼1 THz deviates notably from the experimental observation at finite temperatures. Including the anharmonic phonon renormalization significantly improves the agreement between the experimentally observed [66,67] and theoretically predicted results at 300 and 600 K for this peak.

Because the frequency shifts induced by the bubble diagram are significant [see Fig. 1(c)], neglecting the cubic anharmonicity in anharmonic phonon renormalization is expected to produce remarkable deviations in phonon energies. To comprehensively evaluate this deviation, we calculated the anharmonic phonon dispersions considering only the quartic anharmonicity with/without polarization mixing (PM), as shown in Figs. 2(a) and 2(b), respectively. Indeed, considering only the quartic anharmonicity overpredicts the phonon energies in YbFe$_4$Sb$_{12}$ at finite temperatures, leading to the infinite approach and cross of the avoided-crossing filler modes (Yb-dominated modes) along the Γ-H symmetry path in the Brillouin zone at elevated temperatures, e.g., 600 and 700 K (see Figs. 2(a) and S2 in the SM [46]). If the PM factor was further excluded, even larger overprediction occurs for the phonon energies [see Fig. 2(b)]. This results in a reduction in the scattering rates and thus significant overestimation in lattice thermal conductivity, especially at high temperatures, as illustrated in the subsequent analysis.

When only the quartic anharmonicity is considered, the Sb-dominated intermediate-frequency phonon modes undergo evident stiffening for the majority modes [see Figs. 2(a) and 2(b)]. In contrast, cubic anharmonicity tends to soften the phonons [27,28,44]. This competition eventually results in weak phonon softening for the highest Sb-dominated modes, agreeing well with the experimental observation [67] [see Fig. 1(b)]. Similarly, because of the competition effect induced by the cubic and quartic anharmonicities, the highest Fe-dominated mode exhibits a negligible hardening with increasing temperature, improving the agreement with the experimental observation [67] [see Fig. 1(b)]. Conversely, the Fe-dominated modes possess a significant phonon stiffening by considering only the quartic anharmonicity [see Fig. 2(a)]. Therefore, the cubic anharmonicity cannot be neglected in accurately predicting phonon energies in YbFe$_4$Sb$_{12}$ [44].

We next analyze the localized nature of phonon modes by projecting the participation ratio onto the phonon dispersion curves in the Brillouin zone. As seen in Fig. 3(a), the low-lying flat modes with frequencies ∼1 THz can be identified as localized modes of Yb atoms in the cages [see Figs. 1(a) and 1(b)]. Importantly, the strong anharmonic effect and temperature dependence always exhibit in the low-frequency localized modes [27]. Therefore, to reveal the microscopic origin of the
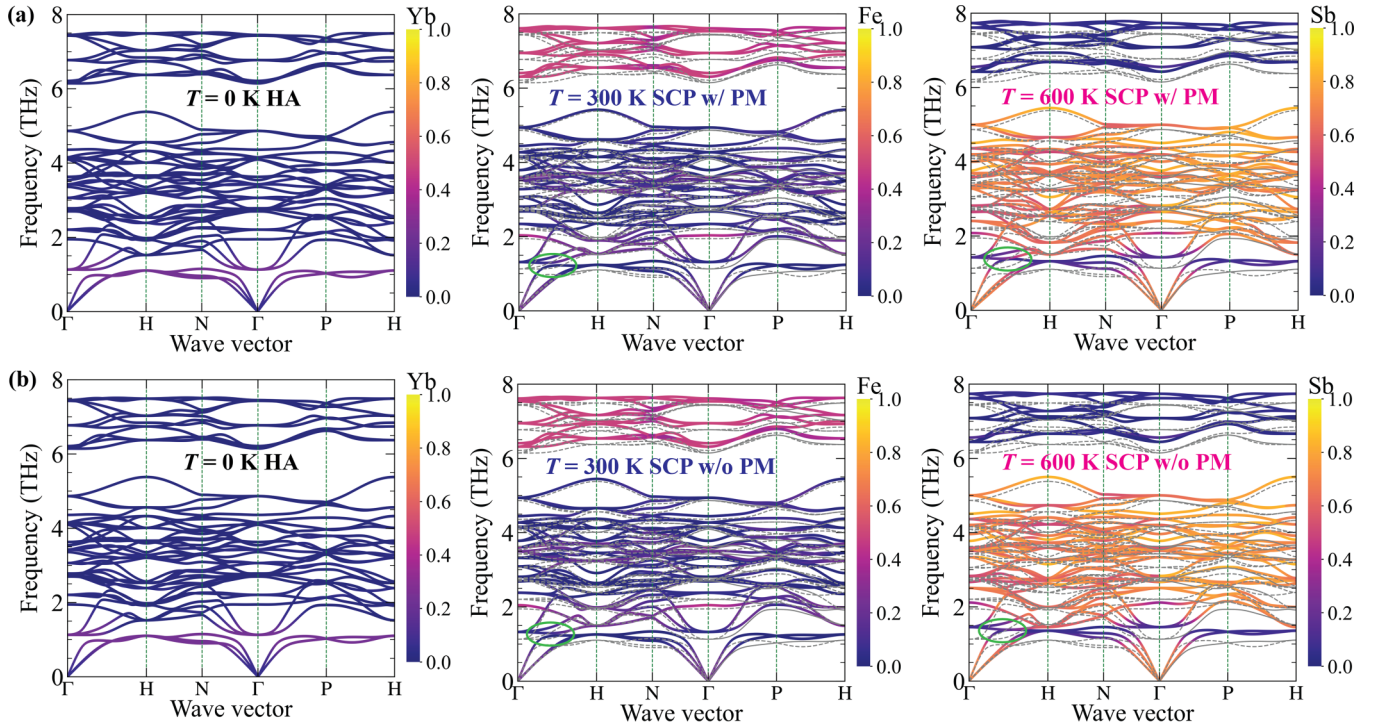
FIG. 2. (a) Calculated phonon dispersion curves along high-symmetry paths in the Brillouin zone. Left panel: Within the harmonic approximation (HA) method, and all bands are colored according to the atomic participation ratio of atom Yb. Middle panel: Within the self-consistent phonon (SCP) theory considering only the quartic anharmonicity at $T = 300$ K, and all bands are colored according to the atomic participation ratio of atom Fe. The dashed lines depict the phonon dispersions calculated using the HA method. Right panel: The same as the middle panel but at $T = 600$ K and the atomic participation ratio of atom Sb. The green circle denotes the infinite approach or cross of the avoided-cross filler modes. PM denotes the polarization mixing (PM). (b) The same as (a) but without considering the PM.

shifts in phonons, we calculated the PESs in real space, which reflects the frequency shifts in reciprocal space [68]. Here, we displace the supercell atoms by $\mathbf{u}_\kappa = \mathbf{M}_\kappa^{-1/2}\mathbf{e}_{q,\kappa}\eta$ [27], where $\mathbf{M}$ and η denote the atomic mass and the amplitude of the normal mode coordinate, respectively, and $\mathbf{e}_{q,\kappa}$ refers to the eigenvector corresponding to the wave vector q and atom κ. As shown in Fig. 3(b), the PESs of the Yb-dominated low-lying flat mode has a deep and flat-bottom U shape, which cannot be well captured by the HA. By further including the higher-order anharmonic terms, i.e., quartic and sextic terms, the PESs from the DFT calculation can be well reproduced, revealing the strong higher-order anharmonic effect in YbFe$_4$Sb$_{12}$. Note that we did not consider the sextic terms in this paper due to their negligible contribution to the PESs [see Fig. 3(b)]. Because of the dominant and positive coupling coefficients of the quartic terms, phonon stiffening arises for the zone center low-lying flat mode [27,68].

Anharmonic phonon renormalization can also largely affect the prediction of atomic MSDs, especially at high temperatures. Figure 3(c) shows that the SCPB calculations reduce the discrepancy in MSD between the theoretical prediction and experimental values [69], especially for the Yb atoms at elevated temperatures. This can be attributed to the suppression of the phonon population from the hardened Yb vibrations. Furthermore, the Yb atoms possess the largest MSD value among all the elements according to both the prediction and experiment [69], indicating the rattling behavior of Yb atoms.

B. Lattice thermal conductivity

With the original/renormalized harmonic and anharmonic IFCs at hand, we calculated lattice thermal conductivity κ_L based on the PBTE method [17,18] and a unified theory of thermal transport [26] with/without considering temperature effect in YbFe$_4$Sb$_{12}$, as shown in Fig. 4(a). The phonon thermal conductivity κ_L^P predicted with the HA method [HA + Boltzmann transport equation (BTE) method], as expected, is seriously underestimated throughout the entire temperature range (300–700 K), like that reported by Li and Mingo [14]. This underestimation could be due to the invalidity of the particlelike phonon picture and/or the neglection of anharmonic phonon renormalization at finite temperatures. We first calculated the coherence contributions within the HA, resulting from the OD based on a unified theory of thermal transport [26]. The inclusion of the coherent terms, i.e., the HA + BTE + OD method, increases κ_L by 38% at 300 K but still fails to reproduce the experimental results [13], implying that the accurate treatment of finite-temperature phonons is necessary.

We then used the SCPB + BTE method to account for the finite-temperature effect induced by the cubic and quartic anharmonicities. The computed κ_L^P using the SCPB + BTE method is significantly enhanced by 61% at 300 K [see the red dash line in Fig. 4(a)], although it is still a bit underestimated compared with the experimental values [13]. The anharmonic phonon renormalization increases the phonon mean free path (MFP), but the MFP of some phonons is still lower than or close to the minimum interatomic distance in YbFe$_4$Sb$_{12}$ (see

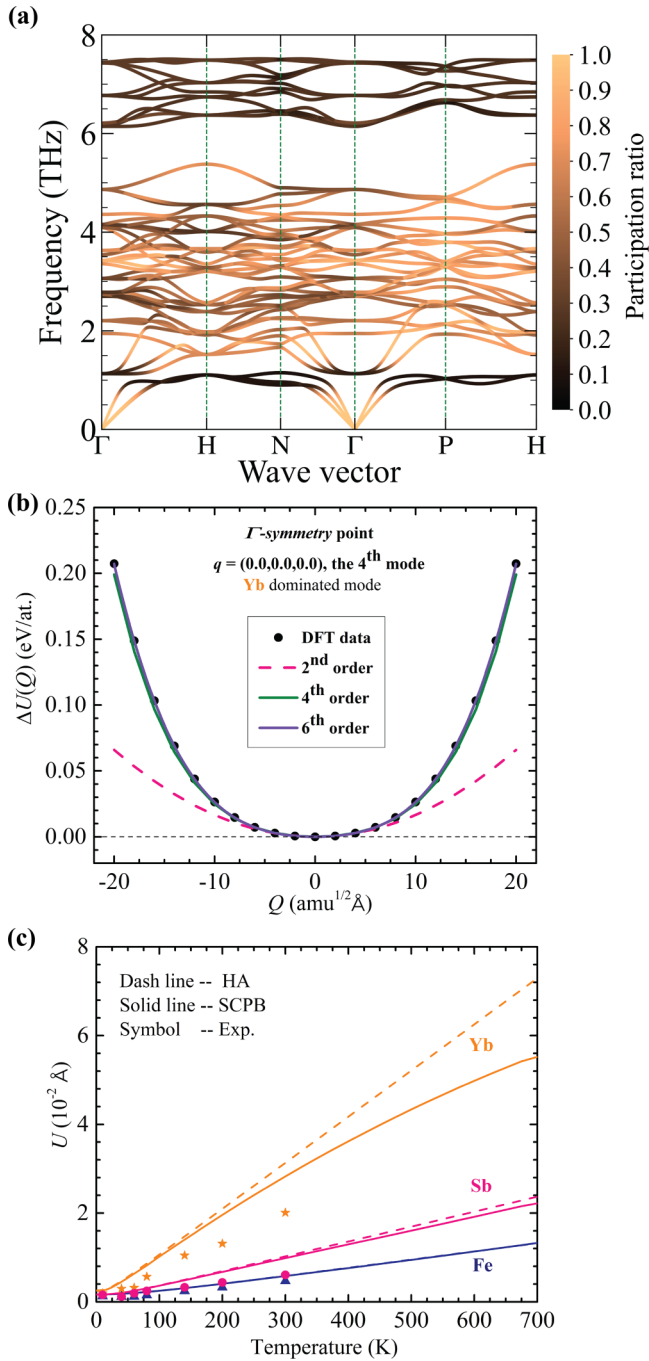**(a)**

(b)

(c)

FIG. 3. (a) Calculated participation ratio projected onto the phonon bands along high-symmetry paths in the Brillouin zone at $T = 0$ K. (b) Calculated potential energy surfaces (PESs) of the fourth mode (low-lying flat mode) at the Brillouin zone center Γ point. The black dot depicts the density functional theory (DFT) data, the red dash line is fitted to the second order, and the solid green and blue lines show the PES decomposed to the fourth and sixth orders, respectively. Note that the third- and fifth-order terms are zero due to the even function property of PESs. (c) Calculated temperature-dependent atomic mean-square displacements (U) within the harmonic approximation (HA; dash lines) and self-consistent phonon + bubble (SCPB; solid lines) approaches compared with those obtained from experiments [69].
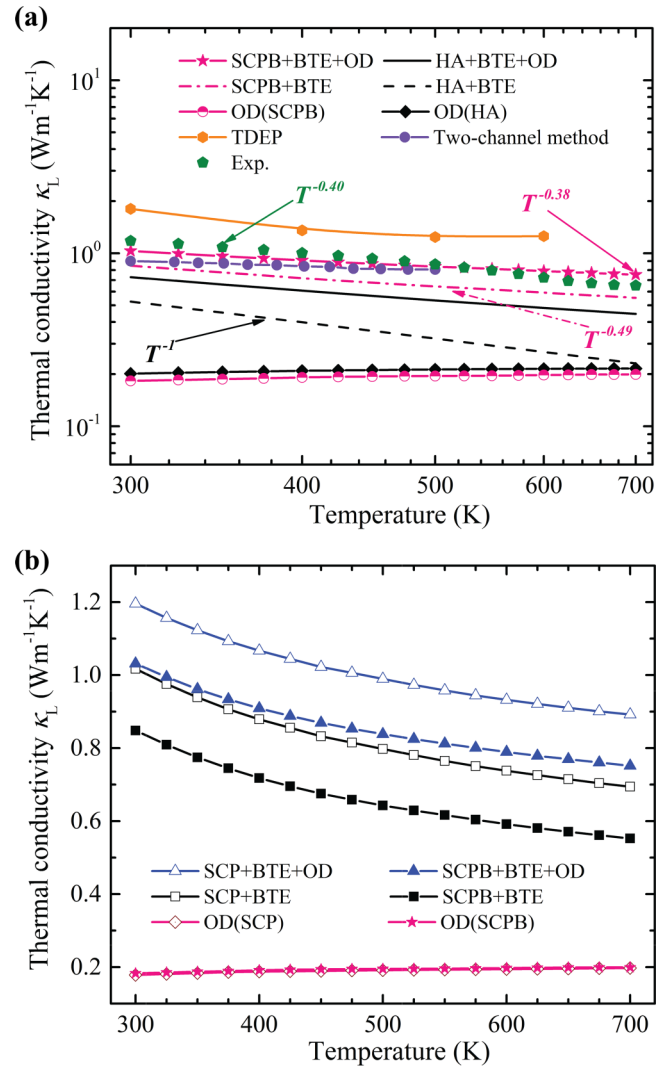
(a)

(b)

FIG. 4. (a) Calculated temperature-dependent lattice thermal conductivity κ_L utilizing different levels of theory including the harmonic approximation (HA)/self-consistent phonon + bubble (SCPB) + Boltzmann transport equation (BTE) and HA/SCPB + BTE + off-diagonal term of heat flux operator (OD) methods in comparison with those obtained from the temperature-dependent effective potential (TDEP) [16], the two-channel method [15], and experiment [13]. In addition, calculated temperature-dependent coherence contributions of κ_P^C (OD) using the harmonic and anharmonic phonon frequencies and eigenvectors are also given in the figure (depicted by the lowest two lines). (b) Calculated temperature-dependent lattice thermal conductivity κ_L using the SCP + BTE method with/without coherence contribution in comparison with that estimated based on the SCPB + BTE + OD method.

Fig. S3 in the SM and the corresponding discussion [46]). By further including the contributions of these phonons to the total thermal conductivity from the OD (coherence contributions), the SCPB + BTE + OD reproduces well the experimental data in the entire temperature range. It is noteworthy that the phonon thermal conductivity κ_L^P comprises, percentage wise, ~82% of the total κ_L at 300 K. Moreover, the temperature dependence of lattice thermal conductivity changes from $\kappa_L^P \sim T^{-1}$ to $\kappa_L^P \sim T^{-0.49}$ by considering only

the anharmonic phonon renormalization and to $\kappa_L \sim T^{-0.38}$ by further including the coherence contribution, which is consistent with the experimental result $\kappa_L \sim T^{-0.40}$. Unlike the prediction in κ_L by the TDEP [16] or the two-channel method [15], the SCPB + BTE + OD method can better explain the experimental observation in YbFe$_4$Sb$_{12}$ without phenomenologically introducing a resonant phonon scattering term or a hopping channel. The above analysis reveals that both the anharmonic phonon renormalization and coherent thermal transport channel are essential in explaining the experimental results and the dominant particlelike nature of phonons in YbFe$_4$Sb$_{12}$.

We have illustrated the significant impact of cubic anharmonicity on phonon energies. To unravel the correlation between the cubic anharmonicity-induced phonon shifts and the resulting change in κ_L, we calculated κ_L using anharmonic phonons with/without considering frequency shifts from the bubble diagram. In Fig. 4(b), the off-diagonal part κ_L^C is insensitive to the phonon shift from the cubic anharmonicity; therefore, the bubble diagram-induced phonon shift only has a significant effect on phonon propagation. This is because the frequency shifts due to the cubic anharmonicity in YbFe$_4$Sb$_{12}$ are no longer negligible, and they can significantly change the phonon scattering rates and the relatively large group velocities of phonon propagation. The computed κ_L by the SCP + BTE + OD method are $\sim 20\%$ higher than those by the SCPB + BTE + OD method. These results highlight the importance of frequency shifts from bubble diagram in the accurate prediction of κ_L in YbFe$_4$Sb$_{12}$.

Recently, the four-phonon scattering process was found to play a crucial role in significantly reducing the phonon scattering rates and thermal conductivity κ_L for many materials [70,71]; however, it has a minor effect on the thermal transport in YbFe$_4$Sb$_{12}$ (see Fig. S4 in the SM and the corresponding discussion for more details [46]). Also, further considering the four-phonon process increases the computational cost by orders of magnitude, we therefore neglect the four-phonon scattering rates in calculating the thermal conductivity, which does not affect our major conclusion in this paper.

C. Particlelike thermal transport channel

To reveal the microscopic origin of the enhancement in κ_L^P due to anharmonic phonon renormalization, we compare the frequency-dependent spectral and cumulative κ_L^P calculated using the harmonic and anharmonic phonon frequencies and eigenvectors. As seen in Fig. 5(a), the lattice heat conduction in YbFe$_4$Sb$_{12}$ is mainly carried by the acoustic and optical phonons with frequencies < 4.5 THz. All the cumulative κ_L^P reaches a plateau corresponding to the dip in the spectral $\kappa_L^P(\omega) \sim 1$ THz, which originates from the low-lying avoided flat modes possessing extremely high scattering rates and low group velocity [see Figs. 5(b) and 5(c)]. Interestingly, the optical modes dominated κ_L^P, e.g., the optical modes contribute 58% to κ_L^P at 300 K (see Fig. S5 in the SM [46]). This phenomenon was also observed in other severely anharmonic materials [25,38].

The increase in κ_L^P calculated by the SCPB + BTE method relative to the HA + BTE method mainly arises from the

acoustic and low-energy optical phonons with frequencies <2.4 THz. Quantitatively, κ_L^P was enhanced by up to a factor of 1.6 and 2.2 at 300 and 600 K, respectively, when the phonons are anharmonically hardened [see Fig. 5(a)]. Particularly, κ_L^P contributed from the first low-energy peak (<1.2 THz) shows around a twofold and threefold increase at 300 and 600 K, respectively. A similar enhancement also occurs in the second Sb-dominated intermediate-frequency peak (1.2–2.4 THz). We will later show that the enhancement in the two abovementioned peaks depends on the behavior of the Yb-dominated modes. In addition, the renormalized phonon κ_L^P without considering frequency shifts from the bubble diagram was also mainly enhanced by the low- and intermediate-frequency phonons <2.4 THz at 600 K [see the bottom panel in Fig. 5(a)]. This observation indicates the strong effect of lattice anharmonicity on low- and intermediate-frequency phonons.

Next, we elucidate the intrinsic effect of the key ingredients in the PBTE equation, i.e., the modal group velocities, mode-specific heat, and scattering rates, on the phonon thermal transport. As shown in Fig. 5(b), the scattering rates from the HA method are strongly suppressed by the anharmonically renormalized phonons, resulting in a remarkable increase in phonon lifetimes and corresponding enhancement in $\kappa_L^P(\omega)$ in the frequency region <4.5 THz [see Fig. 5(a)]. Compared with the change in scattering rates, the phonon group velocities [see Fig. 5(c)] and mode-specific heat (see Fig. S6 and the discussion in the SM [46]) are less affected by anharmonic phonon renormalization. Also, all the scattering rates from the SCPB method are well below the limit of Cahill *et al.* [22] assuming that the maximum scattering rate of a phonon mode is twice its frequency, demonstrating the dominant particlelike nature of phonons in YbFe$_4$Sb$_{12}$.

Furthermore, we calculated the renormalized phonon scattering rates considering only the frequency shifts from the quartic anharmonicity. The scattering rates in Fig. 5(b) considering only the quartic anharmonicity (SCP + BTE) are generally lower than that considering both the cubic and quartic anharmonicities (SCPB + BTE). However, the SCP + BTE method results in substantially higher $\kappa_L^P(\omega)$ in the frequency regime <2.4 THz mainly due to the relatively large group velocity of low-frequency phonons. This result highlights the importance of accurate treatment of the low-frequency modes at finite temperatures.

We also calculated the cumulative κ_L^P as a function of the MFP at 300 and 600 K using the SCPB + BTE method, respectively, as presented in Fig. 5(d). The thermal conductivity is almost saturated when the MFP is >400 nm at both temperatures. The MFPs corresponding to 50% thermal conductivity accumulation from the SCPB calculations are 7 and 6 nm at 300 and 600 K, respectively, indicating the dominance of short-MFP phonons in skutterudite YbFe$_4$Sb$_{12}$. The short MFPs rationalize the weak size effects of thermal conductivity for YbFe$_4$Sb$_{12}$ and suggest small characteristic size is required to suppress its thermal conductivity by nanostructuring.

To understand the microscopic origin of the reduction in scattering rates caused by anharmonic phonon renormalization, we examine the two key ingredients entering the phonon linewidth equation (see Eq. (S7) in the SM
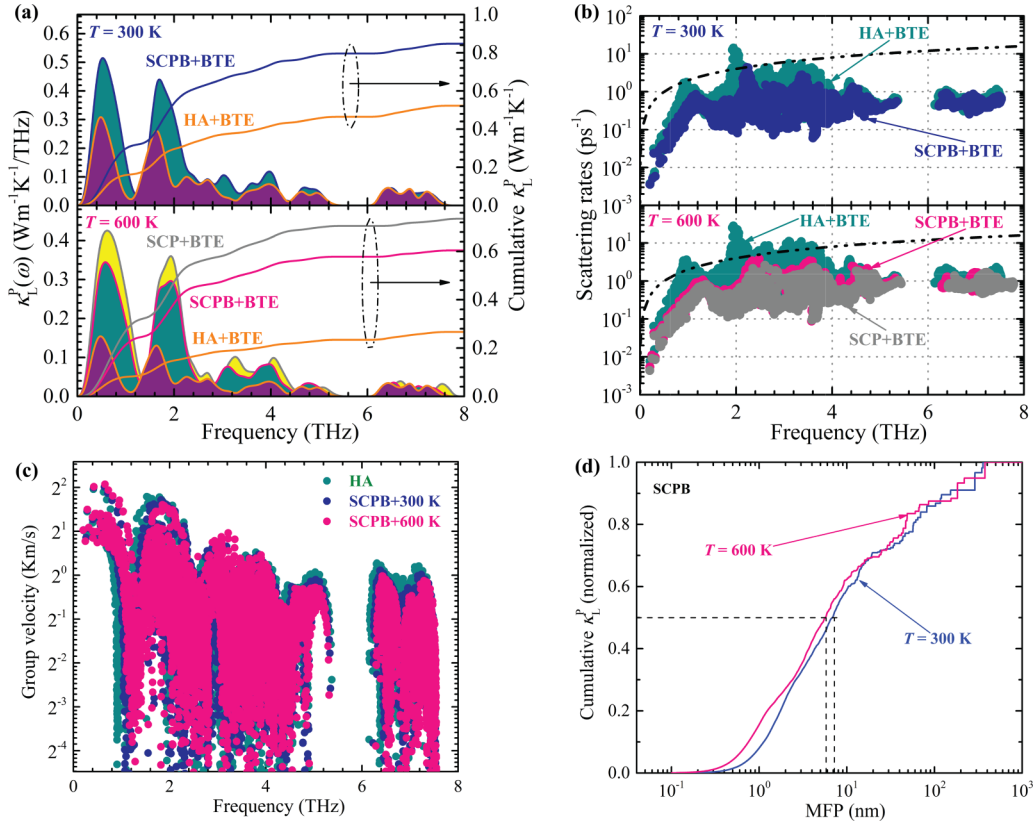
FIG. 5. (a) Calculated spectral and cumulative thermal conductivity with/without considering anharmonic phonon renormalization at $T = 300$ and 600 K. In addition, the calculated renormalized phonon results with/without considering frequency shifts from bubble self-energy were given at $T = 600$ K. (b) Comparison of scattering rates calculated by the harmonic approximation (HA) and anharmonic [self-consistent phonon (SCP), SCP + bubble (SCPB)] phonon frequencies and eigenvectors at finite temperatures (300 and 600 K). The solid black line assumes the scattering rate to be twice the phonon frequency to estimate minimum κ_L [22], the phonon quasiparticle picture becomes valid when the data points are well below this line. (c) Calculated anharmonic renormalization phonon group velocity at finite temperatures ($T = 300$ and 600 K) in comparison with the harmonic phonon group velocity. (d) Calculated cumulative thermal conductivity as a function of mean free paths based on the SCPB method at $T = 300$ and 600 K, respectively.

[46]), namely, the three-phonon cubic coupling strength $|V^{(3)}|^2$ and the SPS. We find that $|V^{(3)}|^2$ and the SPS play different roles in reducing the scattering rates in the different frequency regions. In Fig. 6(a), the anharmonic effect leads to a negligible change in the SPS for phonons <1.2 THz; therefore, the cubic coupling strength is responsible for the suppression in the scattering rates. Figure 6(b) compares $|V^{(3)}|^2$ of the Yb-dominated mode calculated using harmonic and anharmonic frequencies, suggesting that the significant weakening in $|V^{(3)}|^2$ plays a dominant role in decreasing the scattering rates. Furthermore, we note that the dramatic reduction in $|V^{(3)}|^2$ is mainly associated with phonons in frequency regions ∼1 and 2 THz [see Fig. 6(b)], revealing the nontrivial role of the low-lying mode stiffening in suppressing the scattering rates. Similarly, the anharmonic phonon renormalization inducing the reduction in mode Grüneisen parameters mainly occurs in the vicinity of frequency regions ∼1 and 2 THz (see Figs. S7(a)–S7(d) in the SM [46]).

In contrast, the significant shift and reduction in the SPS mainly accounts for the reduction in scattering rates of phonons in the 1.2–2.4 THz frequency interval, as shown in

Fig. 6(a). The peak of the phonon emission process W_q^- results from the low-lying flat modes due to the restriction of the simultaneous energy and momentum conversation, like that illustrated in the literature [14]. Therefore, the corresponding SPS shift can ultimately be traced back to anharmonic phonon stiffening of the Yb-dominated low-lying flat modes, as demonstrated by the similar pace of the SPS shift and the phonon stiffening [see Figs. 1(b) and 6(a)]. Moreover, very little change occurs for $|V^{(3)}|^2$ of phonons with frequency ∼2 THz at the Γ symmetry point as the temperature increases [see in Fig. 6(c)], indicating that the change in the SPS is the major origin of the reduction in scattering rates for phonons within 1.2–2.4 THz. For the phonons within 2.8–4.5 THz, as seen in Fig. 6(a), the evident shift in the SPS plays a dominant role in suppressing the scattering rates due to the negligible change in mode Grüneisen parameter associated with $|V^{(3)}|^2$ (see Figs. S7(a)–S7(d) in the SM [46]).

D. Wavelike thermal transport channel

We next evaluate the coherence contribution to thermal transport by calculating the off-diagonal terms of the heat flux operators. As shown in Fig. 4(a), further including the
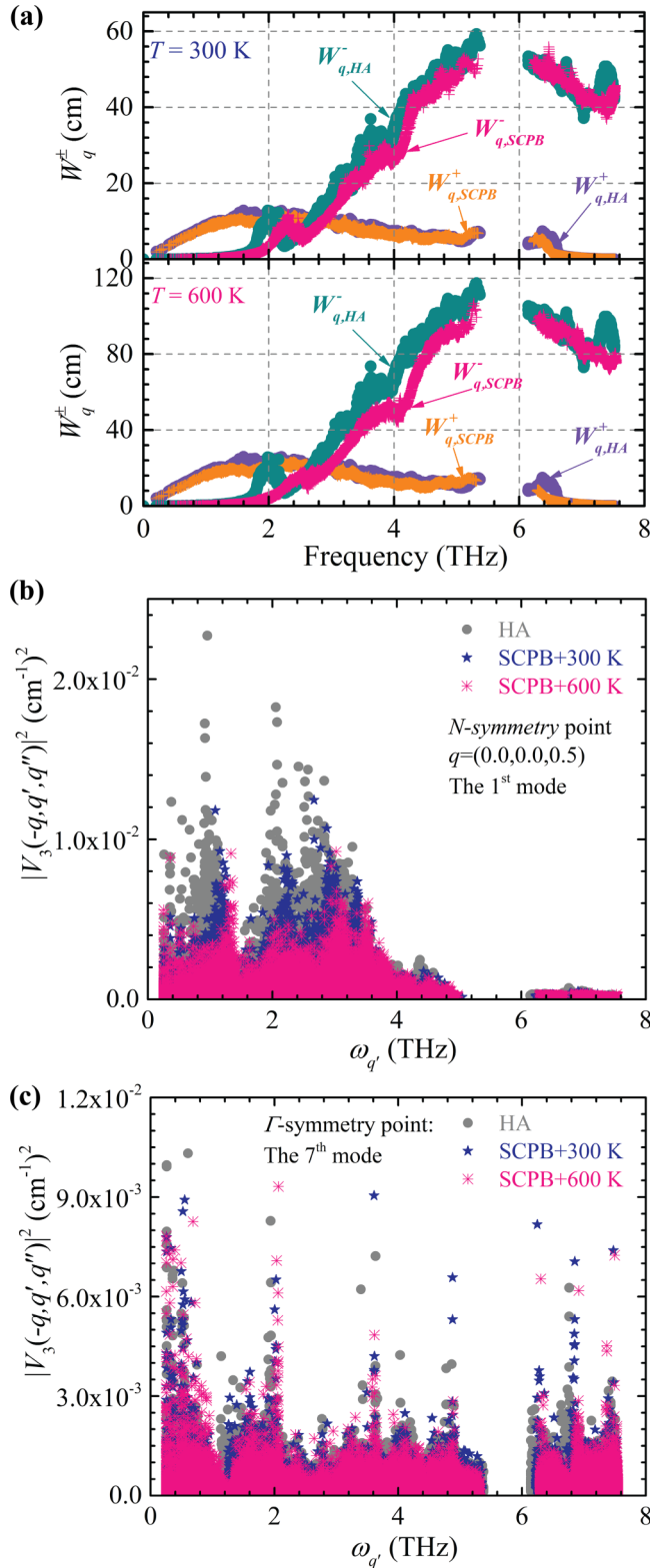
(a)

(b)

(c)

FIG. 6. (a) Calculated energy- and momentum-conserving scattering phase space with/without considering anharmonic phonon renormalization at $T = 300$ and 600 K, respectively. (b) Calculated cubic coupling strength for acoustic phonon mode at the Brillouin zone N-symmetry point [$q = (0.0, 0.0, 0.5)$], with/without considering anharmonic phonon renormalization at $T = 300$ and 600 K as a function of $\omega_{q'}$. (c) The same as (b) but for the seventh phonon mode at the Brillouin zone Γ symmetry point.

coherent transport channel [26] results in better agreement between the calculated κ_L and experiments [13]. In contrast to the decreasing trend in the particlelike phonon contribution κ_L^P, the coherence contribution κ_L^C increases with increasing temperature. Specifically, κ_L^C calculated using the anharmonic phonon frequencies and eigenvectors accounts for 18% of the total κ_L at 300 K and increases to 25% at 600 K, respectively, 22% on average in the entire temperature range [see Figs.4(a) and 7(a)]. This indicates the off-diagonal contribution is no longer negligible due to the strong phonon broadening in YbFe$_4$Sb$_{12}$ [see Fig. 5(b)], although the particlelike phonon channel still dominates the heat transport. However, using the harmonic frequencies and eigenvectors, the coherence contribution κ_L^C contributes up to ~50% of the total κ_L at 700 K [see Fig. 4(a)], although the absolute value of the coherence contribution κ_L^C is insensitive to the anharmonic phonon renormalization [see Figs. 4(a) and 4(c)]. As mentioned earlier, such a high relative contribution is due to the invalidity of the phonon gas model [17,18] within the HA framework, which highlights the importance of the accurate treatment of the anharmonic effect in YbFe$_4$Sb$_{12}$.

To gain a deeper insight into the coherence contribution κ_L^C in YbFe$_4$Sb$_{12}$, we proceed to analyze the spectral $\kappa_L^C(\omega)$ and cumulative κ_L^C considering only the anharmonic phonon stiffening in detail. Contrary to the particlelike phonon transport that κ_L^P is mainly contributed by phonons <2.4 THz [see Fig. 4(a)], phonons in the 2–5 THz interval dominate the coherent thermal transport, as shown in Fig. 7(a). This is due to the strong broadening of phonon states in the intermediate-frequency region in YbFe$_4$Sb$_{12}$, which is beneficial to promote the wavelike tunneling and loss of coherence between vibrational eigenstates from different branches [26]. In Fig. 7(a), phonons with frequencies <3.4 THz are excited up to 300 K, and the higher-energy phonons begin to be excited at elevated temperatures.

We further calculated the modal $\kappa_L^C(\omega_1, \omega_2)$ at 300 and 600 K to show the off-diagonal coupling of vibrational eigenstates. As shown in Figs. 7(b) and 7(c), the quasidegenerate eigenstates ($\omega_1 \cong \omega_2$) contribute most to κ_L^C because a smaller energy difference between eigenstates produces a larger off-diagonal contribution [26,68]. As the temperature increases, the coherence coupling between eigenstates with larger frequency differences becomes stronger (e.g., 4 and 7 THz), resulting in enhanced κ_L^C [see Fig. 7(c)]. The enhancement of the off-diagonal couplings is due to the excitation of high-energy phonons and the larger broadening of phonon eigenstates at high temperatures.

To this end, using a unified theory of thermal transport incorporating population and coherence contributions, i.e., the SCP + BTE + OD model, we can explain well the underlying microscopic mechanism of thermal transport in highly anharmonic YbFe$_4$Sb$_{12}$. However, the theoretically predicted results may be improved by further considering the following factors: (i) using a hybrid functional in DFT calculation, (ii) further thermal expansion with increasing temperature, (iii) further considering the four-phonon interaction process in the phonon scattering rates, and (iv) further including anharmonic contributions of heat flux operators. Note that further including the abovementioned factors into the calculation is extremely computational and time consuming and pro-
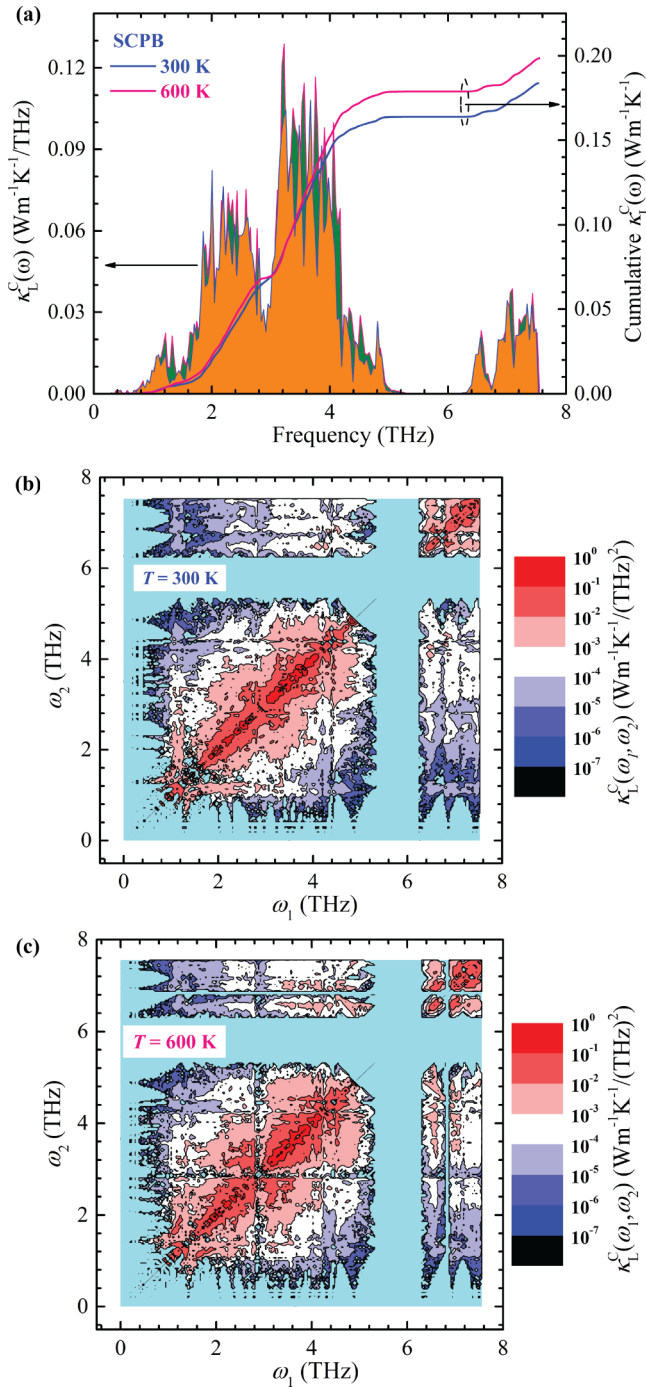
FIG. 7. (a) Calculated spectral and cumulative coherent thermal conductivity using anharmonic phonon frequencies and eigenvectors at $T = 300$ and 600 K, respectively. The contribution of mode j in the coherence couplings between two interbranch modes $(\boldsymbol{q}, j)$ and $(\boldsymbol{q}, j')$ is determined as $c_{\boldsymbol{q}j}/(c_{\boldsymbol{q}j} + c_{\boldsymbol{q}j'})$, where $c_{\boldsymbol{q}j}$ is the mode specific heat. (b) The modal $\kappa_L^C(\omega_1, \omega_2)$ for the contribution to the thermal conductivity of interbranch coherence terms calculated using anharmonic phonon frequencies and eigenvectors at $T = 300$ K. The points on the diagonal, i.e., $\omega_1 = \omega_2$ correspond to degenerate eigenstates. (c) The same as (b) but $T = 600$ K.

hibitive for complex and highly anharmonic compounds based on the current computer configuration and computational techniques. Fortunately, the phonon-phonon scattering selec-

tion rules based on the symmetries of the lattice can be applied to significantly reduce the computational cost and time for four-phonon scattering rates in future study [72].

IV. CONCLUSIONS

In summary, we have systematically investigated the effect of the anharmonicity on phonon vibrational properties and thermal transport by the first-principles-based framework of anharmonic lattice dynamics and a unified theory of thermal transport coupling the population and coherence contributions in YbFe$_4$Sb$_{12}$. We find that both the cubic and quartic anharmonicities are required for accurately describing the anharmonic lattice dynamics. Particularly, the bubble diagram ascribing from the cubic anharmonicity that has been commonly ignored results in significant phonon softening, while the tadpole diagram causes negligible frequency shift. The competition between the phonon stiffening from the loop diagram and the phonon softening from the bubble diagram improves the accuracy in modeling anharmonic lattice dynamics. Particularly, the Yb-dominated low-lying flat modes experience a significant stiffening with increasing temperature due to the strongly anharmonic PESs, consistent with the experimental observation.

Our results show the anharmonic phonon renormalization plays a decisive role in enhancing thermal transport, leading to the dominant particlelike nature of phonons in YbFe$_4$Sb$_{12}$. The anharmonically renormalized phonons not only increase the magnitude of κ_L^P but also change the temperature dependence. Essentially, the enhancement in κ_L^P is mainly due to the significant hardening of the Yb-dominated low-lying modes, which suppresses the cubic coupling strength and alters the SPS. Importantly, we show that the phonon softening due to the cubic anharmonicity enhances the phonon scattering rates, resulting in a 20% reduction in κ_L^P relative to the case considering only the quartic anharmonicity.

Furthermore, we find that the coherence contribution κ_L^C in YbFe$_4$Sb$_{12}$ is nonnegligible, contributing $\sim$22% of the total thermal conductivity throughout the entire temperature range (300–700 K). Here, κ_L^C is insensitive to the anharmonic phonon renormalization and gradually increases with increasing temperature. Also, κ_L^C is mainly contributed by the coherence coupling between two quasidegenerate phonon states within the 2–5 THz frequency interval.

By considering the anharmonic phonon renormalization and coherence contribution, we can reproduce well the experimentally measured κ_L in YbFe$_4$Sb$_{12}$, implying the phenomenological resonant terms or hopping channels may be insignificant. Our results highlight the importance of lattice anharmonicity-induced renormalized phonons in modeling thermal transport in YbFe$_4$Sb$_{12}$. For the materials with strong phonon broadening, the coherent thermal transport channel is also necessary for an accurate description of κ_L. These results offer insights into the microscopic mechanism of thermal transport in filled skutterudites with low-lying flat modes and may help to understand the lattice dynamics and thermal transport in the highly anharmonic complex compounds, e.g., complex thermoelectric materials with ultra-low thermal conductivity, ferroelectric materials, and complex perovskites.

[1] G. A. Slack, in *CRC Handbook of Thermoelectrics*, edited by D. M. Rowe (CRC Press, Boca Raton, FL, 1995), pp. 407–440.

[2] M. Beekman, D. T. Morelli, and G. S. Nolas, Nat. Mater. **14**, 1182 (2015).

[3] G. S. Nolas, M. Kaeser, R. T. Littleton IV, and T. M. Tritt, Appl. Phys. Lett. **77**, 1855 (2000).

[4] W. Li and N. Mingo, Phys. Rev. B **89**, 184304 (2014).

[5] B. C. Sales, D. Mandrus, B. C. Chakoumakos, V. Keppens, and J. R. Thompson, Phys. Rev. B **56**, 15081 (1997).

[6] G. S. Nolas, J. L. Cohn, and G. A. Slack, Phys. Rev. B **58**, 164 (1998).

[7] B. C. Sales, B. C. Chakoumakos, and D. Mandrus, Phys. Rev. B **61**, 2475 (2000).

[8] G. J. Long, R. P. Hermann, F. Grandjean, E. E. Alp, W. Sturhahn, C. E. Johnson, D. E. Brown, O. Leupold, and R. Rüffer, Phys. Rev. B **71**, 140302(R) (2005).

[9] N. R. Dilley, E. J. Freeman, E. D. Bauer, and M. B. Maple, Phys. Rev. B **58**, 6287 (1998).

[10] A. Leithe-Jasper, D. Kaczorowski, P. Rogl, J. Bogner, M. Reissner, W. Steiner, G. Wiesinger, and C. Godart, Solid State Commun. **109**, 395 (1999).

[11] M. B. Maple, E. D. Bauer, N. A. Frederick, P. Ho, W. A. Yuhasz, and V. S. Zapf, Physica B **328**, 29 (2003).

[12] N. R. Dilley, E. D. Bauer, M. B. Maple, S. Dordevic, D. N. Basov, F. Freibert, T. W. Darling, A. Migliori, B. C. Chakoumakos, and B. C. Sales, Phys. Rev. B **61**, 4608 (2000).

[13] P. F. Qiu, J. Yang, R. H. Liu, X. Shi, X. Y. Huang, G. J. Snyder, W. Zhang, and L. D. Chen, J. Appl. Phys. **109**, 063713 (2011).

[14] W. Li and N. Mingo, Phys. Rev. B **91**, 144304 (2015).

[15] S. Mukhopadhyay, D. S. Parker, B. C. Sales, A. A. Puretzky, M. A. McGuire, and L. Lindsay, Science **360**, 1455 (2018).

[16] Y. Wang, H. Yang, W. Qiu, J. Yang, J. Yang, and W. Zhang, Phys. Rev. B **98**, 054304 (2018).

[17] G. P. Srivastava, *The Physics of Phonons* (Routledge, New York, 2019).

[18] R. E. Peierls, *Quantum Theory of Solids* (Clarendon Press, Oxford, 1996).

[19] L. Lindsay, C. Hua, X. L. Ruan, and S. Lee, Mater. Today Phys. **7**, 106 (2018).

[20] T. Tadano, Y. Gohda, and S. Tsuneyuki, J. Phys.: Condens. Matter **26**, 225402 (2014).

[21] A. Einstein, Ann. Phys. **340**, 679 (1911).

[22] D. G. Cahill, S. K. Watson, and R. O. Pohl, Phys. Rev. B **46**, 6131 (1992).

[23] O. Hellman, P. Steneteg, I. A. Abrikosov, and S. I. Simak, Phys. Rev. B **87**, 104111 (2013).

[24] M. M. Koza, M. R. Johnson, R. Viennois, H. Mutka, L. Girard, and D. Ravot, Nat. Mater. **7**, 805 (2008).

[25] T. Tadano, Y. Gohda, and S. Tsuneyuki, Phys. Rev. Lett. **114**, 095501 (2015).

[26] M. Simoncelli, N. Marzari, and F. Mauri, Nat. Phys. **15**, 809 (2019).

[27] T. Tadano and S. Tsuneyuki, Phys. Rev. Lett. **120**, 105901 (2018).

[28] Y. Xia, V. Ozoliņš, and C. Wolverton, Phys. Rev. Lett. **125**, 085901 (2020).

[29] P. E. Blöchl, Phys. Rev. B **50**, 17953 (1994).

[30] G. Kresse and J. Hafner, Phys. Rev. B **47**, 558 (1993).

[31] G. Kresse, J. Furthmüller, and J. Hafner, Phys. Rev. B **50**, 13181 (1994).

[32] G. Kresse and J. Furthmüller, Comput. Mater. Sci. **6**, 15 (1996).

[33] G. Kresse and J. Furthmüller, Phys. Rev. B **54**, 11169 (1996).

[34] J. P. Perdew, K. Burke, and M. Ernzerhof, Phys. Rev. Lett. **77**, 3865 (1996).

[35] A. Möchel, I. Sergueev, H.-C. Wille, J. Voigt, M. Prager, M. B. Stone, B. C. Sales, Z. Guguchia, A. Shengelaya, V. Keppens, and R. P. Hermann, Phys. Rev. B **84**, 184306 (2011).

[36] K. Esfarjani and H. T. Stokes, Phys. Rev. B **77**, 144112 (2008).

[37] E. J. Candès and M. B. Wakin, IEEE Signal Process. Mag. **25**, 21 (2008).

[38] T. Tadano and S. Tsuneyuki, Phys. Rev. B **92**, 054301 (2015).

[39] D. J. Hooton, Philos. Mag. **3**, 49 (1958).

[40] T. R. Koehler, Phys. Rev. Lett. **17**, 89 (1966).

[41] P. Souvatzis, O. Eriksson, M. I. Katsnelson, and S. P. Rudin, Phys. Rev. Lett. **100**, 095901 (2008).

[42] I. Errea, M. Calandra, and F. Mauri, Phys. Rev. B **89**, 064302 (2014).

[43] A. van Roekeghem, J. Carrete, and N. Mingo, Phys. Rev. B **94**, 020303(R) (2016).

[44] T. Tadano and W. A. Saidi, arXiv:2103.00745 (2021).

[45] T. Tadano and S. Tsuneyuki, J. Phys. Soc. Jpn. **87**, 041015 (2018).

[46] See Supplemental Material at http://link.aps.org/supplemental/10.1103/PhysRevMaterials.6.093801 for theoretical background, computational details, DOS, temperature-dependent phonon dispersion curves, calculated phonon MFP, calculated three- and four-phonon scattering rates, relative contribution to lattice thermal conductivity, specific heat, temperature-dependent mode Grüneisen parameters.

[47] A. A. Maradudin and A. E. Fein, Phys. Rev. **128**, 2589 (1962).

[48] R. J. Hardy, Phys. Rev. **132**, 168 (1963).

[49] B. S. Semwal and P. K. Sharma, Phys. Rev. B **5**, 3909 (1972).

[50] D. C. Knauss and R. S. Wilson, Phys. Rev. B **10**, 4383 (1974).

[51] G. P. Srivastava and M. Prasad, Phys. Rev. B **23**, 4273 (1981).

[52] S.-i. Tamura, Phys. Rev. B **27**, 858 (1983).

[53] P. B. Allen and J. L. Feldman, Phys. Rev. B **48**, 12581 (1993).

[54] J. Hafner and M. Krajci, J. Phys. Condens. Matter **5**, 2489 (1993).

[55] P. Hohenberg and W. Kohn, Phys. Rev. **136**, B864 (1964).

[56] J. P. Perdew, K. Burke, and Y. Wang, Phys. Rev. B **54**, 16533 (1996).

[57] F. Zhou, W. Nielson, Y. Xia, and V. Ozoliņš, Phys. Rev. Lett. **113**, 185501 (2014).

[58] H. J. Monkhorst and J. D. Pack, Phys. Rev. B **13**, 5188 (1976).

[59] L. J. Nelson, G. L. Hart, F. Zhou, and V. Ozoliņš, Phys. Rev. B **87**, 035125 (2013).

[60] T. Goldstein and S. Osher, SIAM J. Imag. Sci. **2**, 323 (2009).

[61] A. F. Ioffe and A. R. Regel, in *Progress in Semiconductors*, edited by A. F. Gibson, R. E. Burgess, and F. A. Kröger (Heywood, London, 1960), Vol. 4, pp. 237–291.

[62] Y. Luo, X. Yang, T. Feng, J. Wang, and X. Ruan, Nat. Commun. **11**, 2554 (2020).

[63] Z. Han, X. Yang, W. Li, T. Feng, and X. Ruan, Comput. Phys. Commun. **270**, 108179 (2022).

[64] Y. Tao, Z. Pan, T. Ruch, X. Zhan, Y. Chen, S. X. Zhang, and D. Li, Mater. Today Phys. **21**, 100517 (2021).

[65] W. Schnelle, A. Leithe-Jasper, H. Rosner, R. Cardoso-Gil, R. Gumeniuk, D. Trots, J. A. Mydosh, and Y. Grin, Phys. Rev. B **77**, 094421 (2008).

[66] M. M. Koza, A. Leithe-Jasper, H. Rosner, W. Schnelle, H. Mutka, M. R. Johnson, and Y. Grin, Phys. Rev. B **89**, 014302 (2014).

[67] M. M. Koza, A. Leithe-Jasper, H. Rosner, W. Schnelle, H. Mutka, M. R. Johnson, M. Krisch, L. Capogna, and Y. Grin, Phys. Rev. B **84**, 014306 (2011).

[68] Y. Xia, V. I. Hegde, K. Pal, X. Hua, D. Gaines, S. Patel, J. He, M. Aykol, and C. Wolverton, Phys. Rev. X **10**, 041029 (2020).

[69] M. M. Koza, L. Capogna, A. Leithe-Jasper, H. Rosner, W. Schnelle, H. Mutka, M. R. Johnson, C. Ritter, and Y. Grin, Phys. Rev. B **81**, 174302 (2010).

[70] T. Feng and X. Ruan, Phys. Rev. B **97**, 045202 (2018).

[71] X. Yang, T. Feng, J. Li, and X. Ruan, Phys. Rev. B **100**, 245203 (2019).

[72] A. Cammarata, RSC Adv. **9**, 37491 (2019).